Interfacial pH measurements during CO2 reduction on gold using a rotating ring-disk electrode

Liu, X.; Cecilio de Oliveira Monteiro, M.; Koper, M.T.M.

Check for updates

Interfacial pH measurements during CO$_2$ reduction on gold using a rotating ring-disk electrode†

Xuan Liu, Mariana C. O. Monteiro [ID] ‡ and Marc T. M. Koper [ID] *

Insights into how to control the activity and selectivity of the electrochemical CO$_2$ reduction reaction are still limited because of insufficient knowledge of the reaction mechanism and kinetics, which is partially due to the lack of information on the interfacial pH, an important parameter for proton-coupled reactions like CO$_2$ reduction. Here, we used a reliable and sensitive pH sensor combined with the rotating ring-disk electrode technique, in which a functionalized Au ring electrode works as a real-time detector of the OH$^-$ generated during the CO$_2$ reduction reaction at a gold disk electrode. Variations of the interfacial pH due to both electrochemical and homogeneous reactions are mapped and the correlation of the interfacial pH with these reactions is inferred. The interfacial pH near the disk electrode increases from 7 to 12 with increasing current density, with a sharp increase at around −0.5 V *vs.* RHE, which indicates a change of the dominant buffering species. Through scan rate-dependent voltammetry and chronopotentiometry experiments, the homogenous reactions are shown to reach equilibrium within the time scale of the pH measurements, so that the interfacial concentrations of different carbonaceous species can be calculated using equilibrium constants. Furthermore, pH measurements were also performed under different conditions to disentangle the relationship between the interfacial pH and other electrolyte effects. The buffer effect of alkali metal cations is confirmed, showing that weakly hydrated cations lead to less pronounced pH gradients. Finally, we probe to which extent increasing mass transport and the electrolyte buffer capacity can aid in suppressing the increase of the interfacial pH, showing that the buffer capacity is the dominant factor in suppressing interfacial pH variations.

Leiden Institute of Chemistry, Leiden University, 2300 RA Leiden, The Netherlands.
E-mail: m.koper@lic.leidenuniv.nl
† Electronic supplementary information (ESI) available. See DOI: **https://doi.org/10.1039/d2cp05515e**
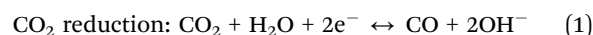‡ Current address: Interface Science Department, Fritz Haber Institute of the Max Planck Society, 14195 Berlin, Germany.
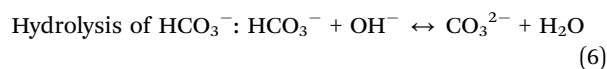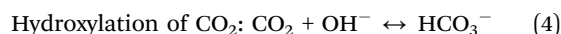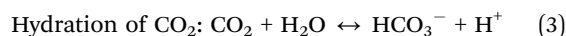
Introduction

The electrochemical conversion of CO$_2$ into high value-added feedstocks is believed to be a promising method to deploy renewable electricity and convert CO$_2$ into useful products. To enhance the reaction activity and selectivity of the electrochemical CO$_2$ reduction reaction (CO$_2$RR) and to suppress the major competing hydrogen evolution reaction (HER), numerous efforts to catalyst improvement have been made over the past decade.[1,2] The electrolyte composition is also an important factor to be reckoned with.[3–5] CO$_2$RR is generally carried out in an alkali bicarbonate electrolyte. Alkali cations,[6–8] bicarbonate,[9–11] and the pH of the electrolyte[12–14] are recognized to influence both CO$_2$RR and HER significantly, and all these variables have been reported to influence the interfacial pH. Therefore, specific information

about the near-surface pH is highly desired to better understand the CO$_2$RR.

Due to the production of OH$^-$ at the interface in neutral and alkaline media (eqn (1) and (2), the thermodynamics and kinetics of both CO$_2$RR and HER change with pH.[15,16]

$$\text{CO}_2 \text{ reduction: } CO_2 + H_2O + 2e^- \leftrightarrow CO + 2OH^- \quad (1)$$

$$\text{Water reduction: } 2H_2O + 2e^- \leftrightarrow H_2 + 2OH^- \quad (2)$$
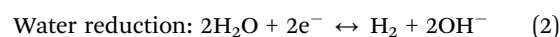
Moreover, there is also a sequence of pH-dependent homogenous reactions taking place, as displayed in eqn (3)–(6):[17,18]

$$\text{Hydration of CO}_2\text{: } CO_2 + H_2O \leftrightarrow HCO_3^- + H^+ \quad (3)$$

$$\text{Hydroxylation of CO}_2\text{: } CO_2 + OH^- \leftrightarrow HCO_3^- \quad (4)$$

$$\text{Protolysis of HCO}_3^-\text{: } HCO_3^- \leftrightarrow CO_3^{2-} + H^+ \quad (5)$$

$$\text{Hydrolysis of HCO}_3^-\text{: } HCO_3^- + OH^- \leftrightarrow CO_3^{2-} + H_2O \quad (6)$$

These homogeneous reactions primarily function as buffer reactions, as CO$_2$ and HCO$_3^-$ can partially consume OH$^-$

This journal is © the Owner Societies 2023

Phys. Chem. Chem. Phys., 2023, **25**, 2897–2906 | 2897

generated from CO_2RR and HER. Still, because of mass transport limitations, OH^- accumulates near the electrode interface, leading to a higher interfacial pH than the bulk value.[19–21] As a result, the interfacial pH determines the interfacial CO_2 concentration, which is directly connected with the CO_2RR rate. Moreover, the local high OH^- concentration affects the local cation concentration, by electroneutrality.[15,22] This local cation concentration has a strong influence on both the CO_2RR and HER rates: alkali cations have been proposed to stabilize certain intermediates of CO_2RR[8] and HER,[15,26] buffer the interfacial pH[7,23] and modify the local electric field.[24,25] The activity for CO_2RR and HER has been reported to increase in the order $Li^+ < Na^+ < K^+ < Cs^+$, which has been attributed to a larger accumulation of Cs^+ at the reaction interface.[7,23] Finally, the interfacial pH determines the local HCO_3^- concentration, and this species contributes to the total hydrogen production through reaction (7):[27]

$$2HCO_3^- + 2e^- \leftrightarrow 2CO_3^{2-} + H_2 \qquad (7)$$
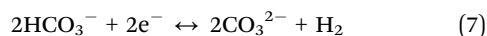
However, since it is difficult to determine the interfacial pH accurately, comprehensive understanding and deconvolution of pH effects from other electrolyte effects are still lacking. On account of the decisive role of the interfacial pH, various techniques have been used throughout the years to measure this key variable,[28] with Scanning Probe Microscopy (SPM) and *in situ* spectroscopy being the most common ones. Due to the high spatial resolution that can be obtained, SPM techniques are very good candidates for measuring the local pH.[29–33] Still, depending on, for example, the feedback used for approaching the surface, pH sensing components may suffer from instability issues.[34,35] Besides, the probe can significantly hinder mass transport, leading to an overestimation of the local pH.[20] Surface-enhanced spectroscopies such as Attenuated Total Reflectance Surface-Enhanced Infrared Absorption Spectroscopy (ATR-SEIRAS) and Surface-Enhanced Raman Spectroscopy (SERS) are also powerful tools for measuring the local pH, in addition to their ability to detect reaction intermediates.[21,36,37] Here, the local pH is normally determined by the ratio of the integrated peak areas between buffer species, *i.e.* CO_2 and HCO_3^-. This would be a reliable pH indicator only if the equilibrium between CO_2 and HCO_3^- was indeed established. However, this is unlikely, as this is the slowest buffering reaction taking place at the interface, as we will discuss further below. Other pH-sensitive molecules can also be introduced as pH probes, though with a risk of perturbing the reactions under consideration.[38]

Developed by Frumkin years ago, the Rotating Ring-Disk Electrode (RRDE) has long been applied as a powerful electroanalytical tool[39] and an ideal real-time detector of products.[40–42] Moreover, due to the convective flow of species induced by the electrode rotation, high rates of mass transport can be well-controlled, facilitating deconvolution of mass transport effects from other electrolyte effects. Albery and Calvo[43] performed pioneering pH measurements using RRDE and developed the corresponding theory as early as 1982. Since then, RRDE pH measurements have been applied to different electrochemical systems.[44–46] Still, the accuracy and sensitivity of the RRDE pH sensor is highly dependent on the pH-sensitive material.

Zhang *et al.*[47] reported pH measurements based on RRDE using the peak potential of CO oxidation on a Pt ring as pH indicator during CO_2RR on the disk. However, there are multiple factors affecting the oxidation of CO on Pt, making it complicated to interpret shifts of the peak potential solely in terms of pH effects.[31,48] More recently, Tackett *et al.*[45] reported a simulation model incorporating electrochemical and buffering reactions to quantify the relationship between the interfacial pH near the ring and the disk electrode of RRDE during CO_2RR. However, each pH data point was measured by recording the open circuit potential (OCP) of an IrO_x-modified ring for 120 s, so that the sensitivity and time resolution of their pH sensor was limited. Besides, the response of the IrO_x pH sensor is largely dependent on the thickness and oxidation state of the IrO_x film[49] and the working conditions, *e.g.*, current density.[44] As a result, only a few pH data points were obtained under steady-state chronopotentiometry conditions on the disk.

To overcome limitations in previous pH measurements, we have developed a highly sensitive voltammetric pH sensor, based on the 4-hydroxylaminothiophenol/4-nitrosothiophenol (4-HATP and 4-NSTP) redox couple, whose peak potential shows a Nerstian shift with pH over a broad pH range.[20,31,32] Recently, we have combined this redox couple to a RRDE system by modifying a gold ring with the pH probe. Feasibility and versatility of the 4-HATP/4-NSTP modified RRDE pH probe in different electrolytes were validated by measuring the interfacial pH during HER on a gold disk.[42] The time scale of the pH sensor depends on the scan rate with which the redox couple is measured. In this work, the redox couple was cycled within a 400 mV potential window at 200 mV s^{-1}, so that the pH is measured every 4 s.

Here, we apply the RRDE pH probe to estimate the interfacial pH during CO_2RR on a gold electrode. Coupled with the highly sensitive and stable voltammetric pH sensor (4-HATP/4-NSTP), with RRDE we can record the variation of interfacial pH in a broad potential range with high accuracy. We have compiled the advantages of our pH sensor compared to previous literature in the ESI† (Table S1). Because of the good time resolution of our sensor, we can test the level of equilibration of the homogeneous buffer reactions during cyclic voltammetry. This unique method provides a definite correlation of interfacial pH with mass transport, and other electrolyte effects such as ionic strength and cation identity. Our measurements in different electrolytes prove the buffering effect of cations, and show how the role of mass transport and buffer capacity on CO_2RR is closely related to interfacial pH changes. We will argue that the insights obtained here are relevant to other electrode materials and geometries as well.

Results and discussion

Interfacial pH measurement with RRDE

The details of using RRDE with the voltammetric pH sensor on the ring are given in our previous paper[42] and in the ESI.† Briefly, the interfacial pH measured at the ring can be converted to the corresponding interfacial pH at the disk using the

2898 | *Phys. Chem. Chem. Phys.*, 2023, **25**, 2897–2906

This journal is © the Owner Societies 2023

equations developed by Albery and Calvo, also taking into account the buffering reactions taking place in the electrolyte. The relevant mathematical equations are given in the ESI,† as well as a discussion of the expected accuracy of the calculated disk pH. We also note that our aim with this method is not to claim absolute accuracy of individual pH values (also because in reality the pH near the disk is not a constant as there is not a perfectly homogeneous current distribution), but rather to evaluate semi-quantitative changes in the interfacial pH values during cyclic voltammetry in different electrolytes with different parameters, such as buffering strength, cation identity, and rate of mass transport. As mentioned in the Introduction, the very distinct advantage of using RRDE for performing such measurements is that in this setup, the pH measurement does not disturb the interfacial environment as the pH probe is remote from the interface itself (a typical diffusion layer thickness under our conditions is 12.24 μm (detailed calculation in the ESI†), while the ring electrode is 1.5 mm away from the disk electrode.). Therefore, we expect the results to be identical to configurations where the pH probe is absent.

Variation of the interfacial pH during CO_2RR

The interfacial pH of the Au disk is measured while cycling the electrode slowly at 2 mV s^{-1} from 0 to −1.0 V vs. RHE. The increase in current density with potential leads to an increasing generation of OH$^-$ near the surface of the electrode (Fig. 1(a)). As a result, the interfacial pH rises considerably with current density (Fig. 1(b)), despite the high electrode rotation rate (2500 rpm) and the buffering from both CO_2 and HCO_3^-. According to the pH recorded, the potential and current density range from Fig. 1 can be divided into two regions, each dominated by a different buffer. At less negative potentials and lower current densities (red shaded region in Fig. 1), only a small change in pH is detected and the interfacial pH stabilizes around 7 (bulk pH 6.8). With the rise in current density at around −0.5 V, the pH increases drastically from 7 to 9, suggesting a change in

interfacial environment. At even more negative potentials and current densities (blue shaded region in Fig. 1), the pace of the pH variation slows down again despite the high and increasing current. This is in agreement with the results from Tackett et al.,[45] though our measurements have a higher time and pH resolution owing to the advantages mentioned above.

There are two buffers in CO_2-saturated bicarbonate electrolyte: according to the Henderson–Hasselbalch equation (pH = pK_a + log([A$^-$]/[HA])), where HA is the acid and A$^-$ is its conjugated base),[50] the buffer range of CO_2/HCO_3^- is 5.35–7.35 (pK_{CO_2/HCO_3^-} = 6.35), while it is 9.33–11.33 for HCO_3^-/CO_3^{2-} (p$K_{HCO_3^-/CO_3^{2-}}$ = 10.33). Once the interfacial pH during CO_2RR exceeds the buffer range, [HA] is too low and the buffer breaks down. Therefore, the increase of interfacial pH from 7 to 9 marks the breakdown of the CO_2/HCO_3^- buffer and the onset of the HCO_3^-/CO_3^{2-} buffer. Since the interfacial pH influences the corresponding reactions and their kinetics (see Introduction), this substantial pH change is expected to be a turning point for both the homogenous reactions and the electrochemical reactions.

Equilibrium of the homogenous reactions

As mentioned above, the CO_2/HCO_3^- couple buffers through either the hydration or hydroxylation pathways (eqn (3) and (4)), while HCO_3^-/CO_3^{2-} buffers through either the protolysis or the hydrolysis pathways (eqn (5) and (6)).[17,18] By comparing the reaction rates given by eqn (8)–(11), the hydration reaction (eqn (3)) is the main buffering reaction in the CO_2/HCO_3^- working region here (at pH 5–7), while the hydrolysis pathway (eqn (6)) dominates in the HCO_3^-/CO_3^{2-} buffering region here (at pH 9–11) (k_{3+} to k_{6+} have been reported as 0.037 s^{-1}, 2.23 × 10^3 M^{-1} s^{-1}, 59.4 s^{-1}, 6.0 × 10^6 M^{-1} s^{-1}, respectively).[18]

$$r_{3+} = k_{3+}[CO_2] \tag{8}$$

$$r_{4+} = k_{4+}[CO_2][OH^-] \tag{9}$$

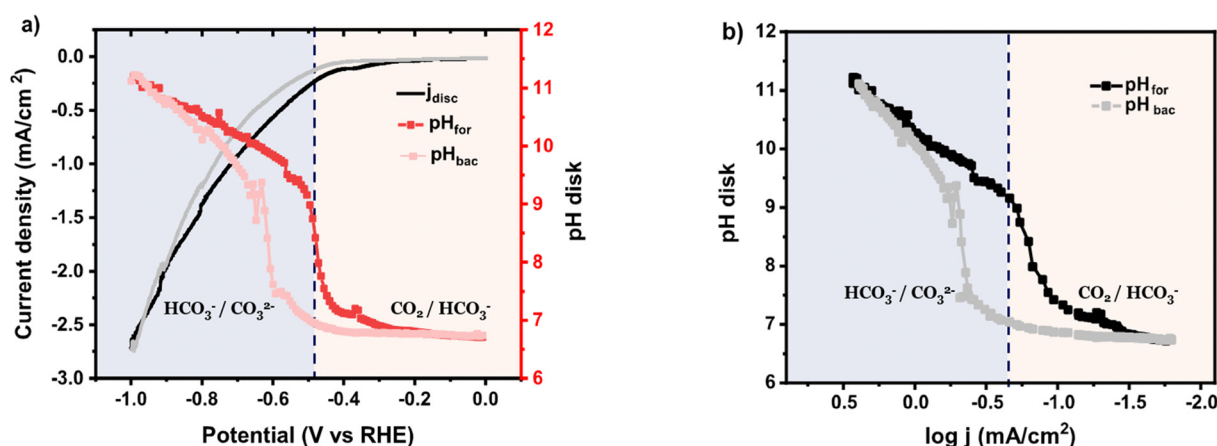$$r_{5+} = k_{5+}[HCO_3^-] \tag{10}$$

Fig. 1 (a) Variation of the interfacial pH recorded during cyclic voltammetry in CO_2-saturated 0.1 M $NaHCO_3$ at 2 mV s^{-1} and a rotation rate of 2500 rpm: the solid line is the current density with the forward and backward scans in black and grey, respectively, while the red and pink curves refer to the corresponding interfacial pH during the forward and backward scan, respectively. (b) Interfacial pH as function of the logarithm of the current density during the cyclic voltammetry from (a). Potentials in all figures have been converted to the RHE scale using the bulk pH.

This journal is © the Owner Societies 2023

Phys. Chem. Chem. Phys., 2023, **25**, 2897–2906 | **2899**

$$r_{6+} = k_{6+}[\text{HCO}_3{}^-][\text{OH}^-] \qquad (11)$$

Based on these rate constants, the equilibrium between $\text{HCO}_3{}^-$ and $\text{CO}_3{}^{2-}$ should be established within microseconds,[17,20] while it takes on the order of 10 s to reach equilibrium for the $\text{CO}_2/\text{HCO}_3{}^-$ buffer at pH 5.35–7.35 due to the slow hydration of CO_2 (these equilibration times are estimated from literature parameters[17]). During the measurements, a slow scan rate of 2 mV s^{-1} is applied to the disk electrode to minimize the disturbance of the system and the pH is recorded every 4 s, which is compatible with this timescale. This makes it reasonable to assume that all buffering reactions are in equilibrium at this scan rate. To confirm the validity of this equilibrium assumption, variations of interfacial pH were recorded as a function of the scan rate of the disk electrode, in CO_2-saturated bicarbonates. As shown in Fig. S4b (ESI†), the interfacial pH increases with the scan rate. However, since the current density increases with the scan rate as well (Fig. S4a, ESI†), this also contributes to the increase of interfacial pH. To deconvolute the impact from current density and scan rate, similar experiments were performed in CO_2-saturated acidic perchlorates. As shown in Fig. 2, the proton reduction reaction reaches its diffusion limited plateau (Fig. 2(a)) from -0.6 V vs. RHE. The current densities of these diffusion-controlled plateaus are independent of scan rates, so that interference from current density is avoided. Besides, the corresponding interfacial pH of these plateaus is around 7 (Fig. 2(b)), which is within the buffer range of $\text{CO}_2/\text{HCO}_3{}^-$, making the plateau a window to study the CO_2 hydration pathway at different time scales (using different scan rates). As the scan rate is increased from 2 mV s^{-1} to 20 mV s^{-1}, no obvious change in the interfacial pH plateaus is found, in agreement with the corresponding current density plateaus. However, at scan rates higher than 10 mV s^{-1}, the first few data points of interfacial pH, recorded just before reaching the plateau, are slightly higher, which indicates that the homogeneous reactions have not yet reached equilibrium. This agrees well with the relaxation times mentioned above: it takes $\sim$12 seconds (3 data points, corresponding to 24 mV for 2 mV s^{-1}, but to 120 mV for 10 mV s^{-1}) for the interfacial pH to equilibrate to the plateau value (pH = 7). For scan rates lower than 5 mV s^{-1}, this slow equilibration

is not observed, demonstrating that the homogeneous reactions can be considered to be in equilibrium in the $\text{CO}_2/\text{HCO}_3{}^-$ buffering region.

Chronopotentiometry experiments at different current densities were also conducted, under the same conditions. CO_2RR on the disk is turned "on" and "off" every 2 minutes while the variation of pH is constantly measured at the ring. Since $\text{CO}_2/\text{HCO}_3{}^-$ buffers until pH 7.35, according to Fig. 2(c), $\text{CO}_2/\text{HCO}_3{}^-$ buffers when the current density is smaller than 2.8 mA cm^{-2} (pink region), while $\text{HCO}_3{}^-/\text{CO}_3{}^{2-}$ buffering becomes dominating thereafter. At current densities between 0.3–2.3 mA cm^{-2} an initial increase of the interfacial pH is observed, followed by a decrease reaching a plateau. This is highlighted in the insets of Fig. 2(c). This illustrates that $\text{CO}_2/\text{HCO}_3{}^-$ takes a few seconds to equilibrate and, remarkably, this process is recorded by the pH sensor. In fact, this transient increase in local pH has also been detected using SECM in our previous work.[20] By contrast, for $\text{HCO}_3{}^-/\text{CO}_3{}^{2-}$ buffering region (current density equal or higher than 2.8 mA cm^{-2}), such transient increase is not expected, as the $\text{HCO}_3{}^-/\text{CO}_3{}^{2-}$ equilibrium is reached within microseconds. However, we could not observe that in the data here due to the disturbance caused by H_2 bubbles at these currents.

Speciation of the electrolyte at the CO_2RR interface

As CO_2 is continuously purged into the electrolyte during the measurements, the total carbon concentration (TC, eqn (S7) in the ESI†), which is the sum of the concentrations of the intrinsic (bi-)carbonate electrolyte and the saturated CO_2 concentration from extrinsic bubbling, stays constant.[51] However, the distribution of the various carbonaceous species (i.e. CO_2, $\text{HCO}_3{}^-$, and $\text{CO}_3{}^{2-}$) near the surface alters as a function of the interfacial pH, which is in turn a consequence of the CO_2RR and the concurrent homogeneous reactions. As the homogeneous reactions can be considered to be in equilibrium, the interfacial concentrations of the carbonaceous species can be obtained by working out the equilibrium equations (eqn (S8)–(S10) in the ESI†), so that variation of these concentrations during CO_2RR can be traced in real time (Fig. 3). In the $\text{CO}_2/\text{HCO}_3{}^-$ buffering region, the concentration of CO_2 decreases sharply as it is consumed both as
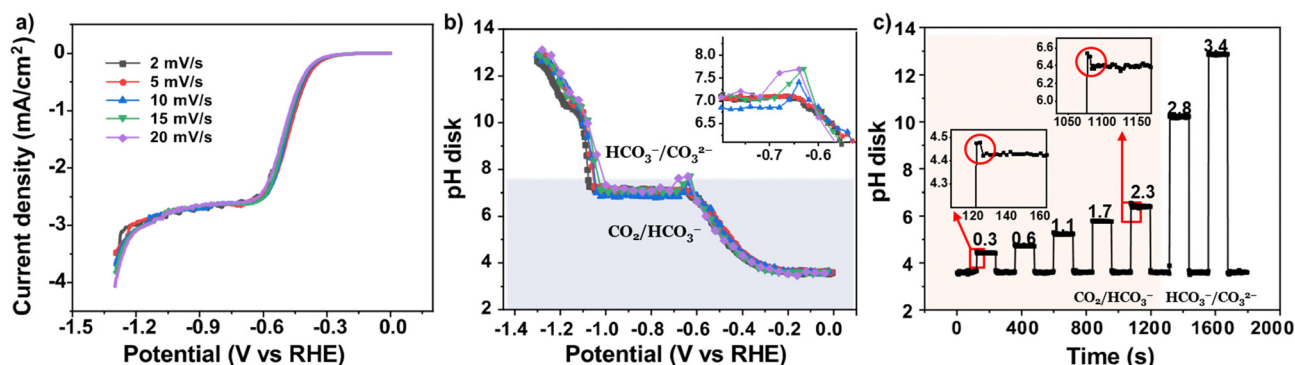

Fig. 2 (a) Cyclic voltammograms in CO_2-saturated 30 mM NaClO$_4$ (pH = 3, acidified with 1 mM HClO$_4$) at different scan rates. (b) Variation of the interfacial pH as a function of potential during the cyclic voltammetry from (a). (c) Variation of the interfacial pH during chronopotentiometry in the same electrolyte, where CO_2RR on the disk electrode is turned "on" and "off" at different current densities (shown above the plot, in mA cm^{-2}) every 2 minutes. The rotation rate of RRDE is 2500 rpm.

2900 | *Phys. Chem. Chem. Phys.*, 2023, **25**, 2897–2906

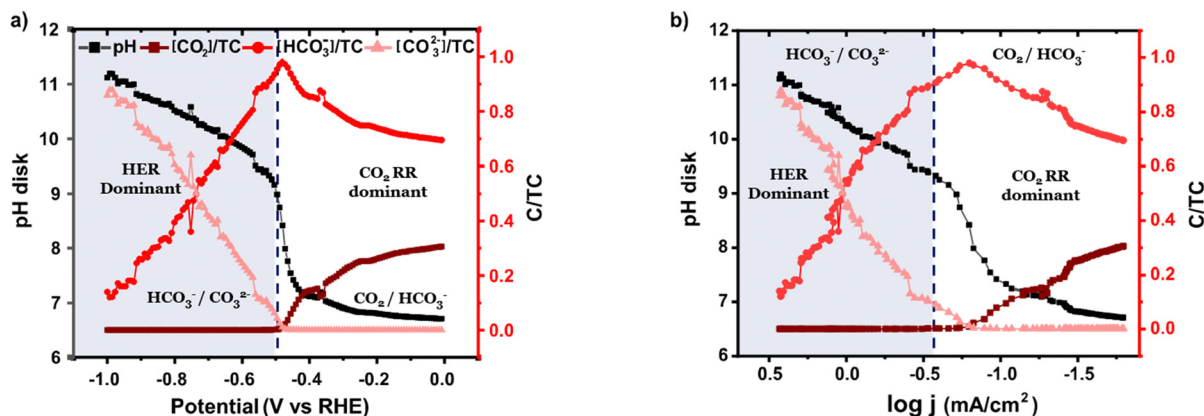This journal is © the Owner Societies 2023

Fig. 3 Variation of concentrations of carbonaceous species with (a) potential and (b) logarithm of the current density. The concentrations are calculated from the measured pH from Fig. 1, using the equilibrium equations. TC is the total concentration of all the carbonaceous species. The black curve reports the measured pH and the red shades the concentrations of each species normalized to TC.

an electrochemical reactant and as a buffer reagent. The concentration of HCO_3^- increases, while there is only a trace amount of CO_3^{2-}. As the interfacial pH rises, the interfacial CO_2 becomes exhausted, the concentration of HCO_3^- near the electrode starts to decay, while the concentration of CO_3^{2-} increases, as illustrated in Fig. 3. Noteworthily, the depletion of interfacial CO_2 by the end of the CO_2/HCO_3^- buffering region does not mean that the CO_2RR is diffusion limited. Instead, as a bifunctional species, a significant amount of CO_2 is consumed by the buffering reactions instead of by CO_2RR. For every CO_2 molecule reduced, two OH^- are produced, which consume CO_2 for buffering. Simultaneously, the competing water reduction reaction also produces $2OH^-$ and consumes CO_2 for buffering. This self-consumption of CO_2 largely limits the reaction rate of CO_2RR, which explains why the reaction never reaches its theoretical diffusion limited current density (101.4 mA cm^{-2} in the case of 2500 rpm, detailed calculations are in the ESI†). This is a key intermediate conclusion, which we have drawn previously and now have quantitative pH data supporting it:[52] under conditions of high mass transport, CO_2RR is never close to being mass transport limited. All relevant mass transport effects under these conditions are related to interfacial pH gradients.

Therefore, the local concentrations of the carbonaceous species can be estimated from the local pH.

Interfacial pH and mass transport

Previous work has shown that the faradaic efficiency of CO_2RR on Au increases with rotation rate, mainly because of suppression of the competing water reduction reaction.[11] A decrease in the interfacial pH by enhanced mass transport has been assumed to be the underlying reason, since the water reduction reaction is favored by alkalinity.[15,53] To verify this effect, variation of the interfacial pH is recorded under different rotation rates. The results show that the interfacial pH lowers by one unit as the rotation increases from 1000 rpm to 2500 rpm (Fig. 4(b) and (c)), as the OH^- generated by CO_2RR and HER is transported away from the interface faster with increasing rotation. Increasing mass transport decreases the interfacial pH, and thereby enhances the selectivity towards CO_2RR by slowing down the water reduction reaction. This explains the subtle change of total current density with increasing rotation rate (Fig. 4(a)): both CO_2RR and water reduction are affected by the decreased interfacial pH. The water reduction reaction is slowed down while CO_2RR is slightly favored.[26] Remarkably, as a result of the fast generation of OH^-,

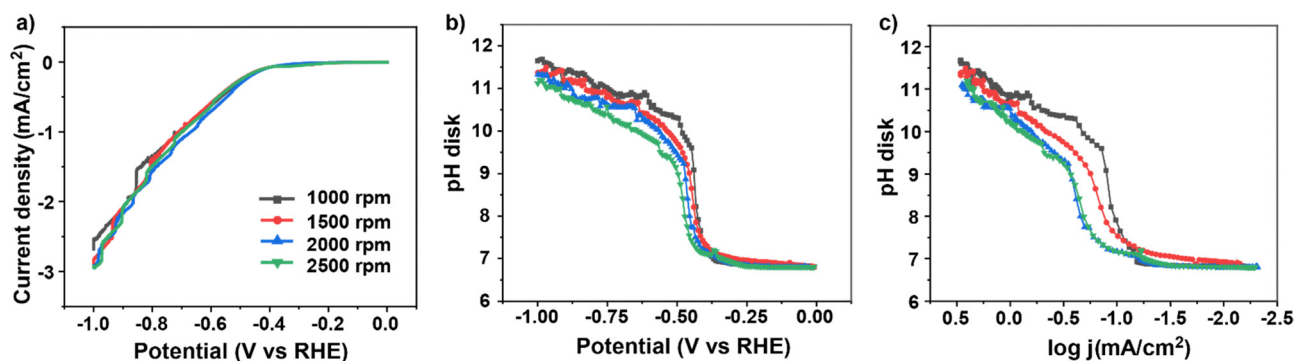Fig. 4 (a) Cyclic voltammograms under different rotation rates in CO_2 saturated 0.1 M NaHCO₃ at 2 mV s^{-1}. Variation of the interfacial pH as a function of (b) potential and (c) the logarithm of the current density during the cyclic voltammetry from (a).

This journal is © the Owner Societies 2023

Phys. Chem. Chem. Phys., 2023, 25, 2897–2906 | 2901

the interfacial pH is still 4 units larger than the bulk value under the highest rotation rate, highlighting the large difference between the interfacial environment and the bulk phase, and the relatively limited effect that enhancing mass transport has in suppressing this difference.

Interfacial pH and buffer capacity

As mentioned before, the concentration of bicarbonate buffer is expected to strongly affect the interfacial pH. To probe the variation of the interfacial pH in electrolytes with different buffer capacities, measurements were performed in CO_2-saturated bicarbonate electrolyte containing different bicarbonate concentrations. The cation concentration is kept constant at 0.5 M by adding appropriate amounts of sodium perchlorate, to deconvolute the effects from bicarbonate and cation concentration. Fig. 5(a) shows that the current density is largely enhanced with increasing bicarbonate concentration, which is primarily due to the increasing bicarbonate reduction (eqn (7)).[27] Still, thanks to the efficient buffer ability of bicarbonate, the interfacial pH decreases significantly from 11 to 9 in the HCO_3^-/CO_3^{2-} buffering range with increasing buffer capacity (Fig. 5(b)), even with more OH^- being generated due to the higher current density. This is in agreement with the results from Tackett et al.:[45] the variation of the interfacial pH becomes less pronounced and less intense in 0.5 M $KHCO_3$. When plotting as a function of current density (Fig. 5(c)), the decrease of interfacial pH with increasing buffer capacity is

even more pronounced. Instead of a sudden change in pH as observed in a weakly buffered environment, the variation of pH happens at a lower rate with a higher concentration of bicarbonate. Fig. 5(d) displays the evolution of the relative concentration of CO_2 compared to total carbon with current density. Despite a similar interfacial concentration of CO_2 at low potentials, compared with more weakly buffered electrolytes, the pH in strongly buffered electrolytes evolves much slower, so the exhaustion of interfacial CO_2 is postponed. Importantly, by comparing Fig. 4 and 5, we can conclude that a suppression of interfacial pH gradients is more effectively achieved by buffering than by improving mass transport. However, as mentioned above, a higher bicarbonate concentration will also promote H_2 production, due to eqn (7), and hence the FE towards CO_2RR products may still be negatively affected.

Interfacial pH and cation effect

As mentioned in the Introduction, the rate of CO_2RR varies with different alkali cations, which has been suggested, among other things, to be related to their different buffering ability.[23] To verify this, the interfacial pH is monitored during CO_2RR in CO_2 saturated bicarbonates with different alkali cations. The current density here increases in the order: $Li^+ < Na^+ < K^+ < Rb^+ < Cs^+$ (Fig. 6(a)), in agreement with the results reported in the literature.[8] This increase from Li^+ to Cs^+ is ascribed to the enhancement of both CO_2RR and HER, due to a stronger tendency to interact and stabilize the negatively charged

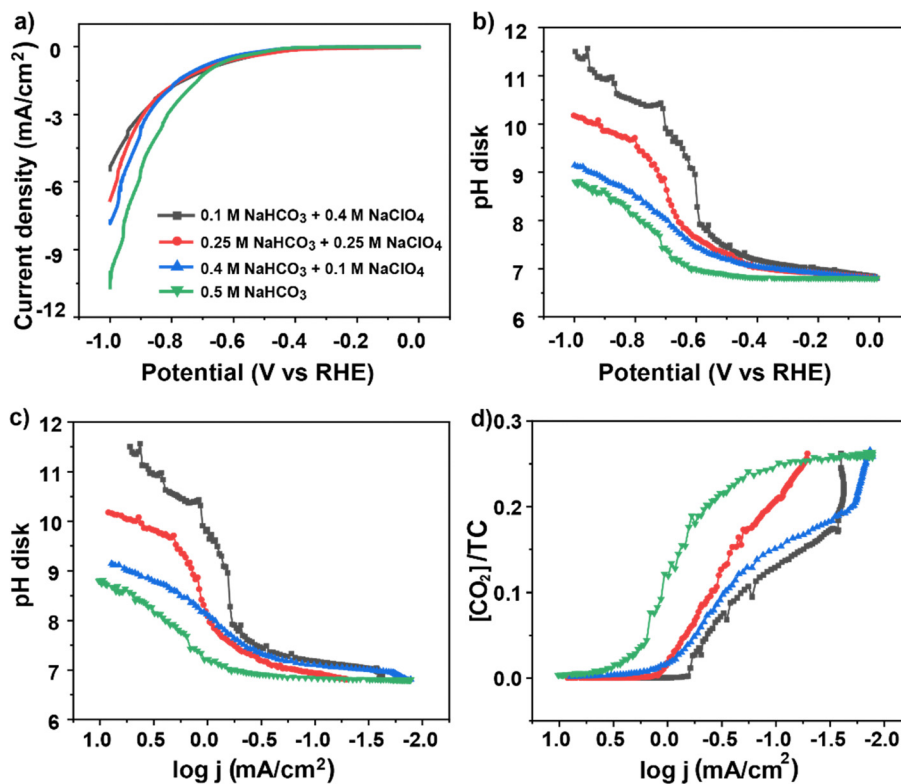Fig. 5 (a) Cyclic voltammograms in CO_2-saturated bicarbonate electrolytes with increasing buffer capacity, at 2 mV s^{-1} and a rotation rate of 2500 rpm. Variation of the interfacial pH as a function of (b) potential and (c) the logarithm of the current density. (d) The calculated concentrations of CO_2 during the cyclic voltammetry from (a).

2902 | *Phys. Chem. Chem. Phys.*, 2023, **25**, 2897–2906

This journal is © the Owner Societies 2023

Fig. 6 (a) Cyclic voltammograms in 0.1 M CO_2-saturated bicarbonate electrolytes with different cations, at 2 mV s^{-1} and a rotation rate of 2500 rpm. Variation of the interfacial pH as a function of (b) potential and (c) the logarithm of the current density. (d) The calculated concentrations of CO_2 during the cyclic voltammetry from (a).
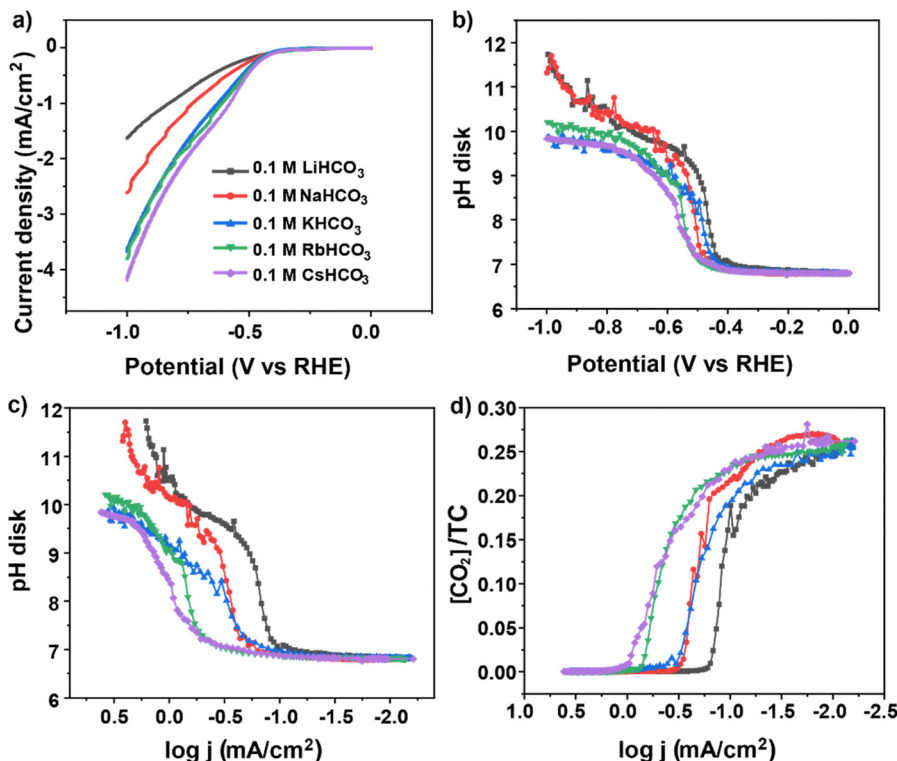
reaction intermediate of CO_2RR and HER and a higher interfacial concentration of Cs$^+$.[8,15] The results in Fig. 6(b) show that the interfacial pH decreases from Li$^+$ to Cs$^+$, demonstrating the different buffering effect of the cations with high sensitivity and pH resolution. According to Singh et al.,[23] the buffering ability of cations originates from the hydrolysis of the water molecules from the cation's hydration shell: once the pH around the cation reaches its pK_a, a hydronium ion will be generated. However, the trend in Fig. 6(b) is clearly less pronounced compared to, for example, the effect of the bicarbonate buffer. Further increase of pH at high current densities is found for Li$^+$

and Na$^+$ (Fig. 6(c)), attributed to a breakdown of the weak buffering capacity of Li$^+$ and Na$^+$ compared with the other cations. The variation of CO_2 concentration is shown in Fig. 6(d). Starting at a nearly identical initial value, a larger cation such as Cs$^+$ exhibits a stronger resistance to the pH variation, leading to a longer retention of the interfacial CO_2 concentration.

To further test the buffer ability of alkali cations, the same experiments were conducted in a 0.1 M bicarbonate electrolyte with independently increasing the concentration of Na$^+$ by adding NaClO$_4$. The results illustrate that the current density increases with the cation concentration while the interfacial pH
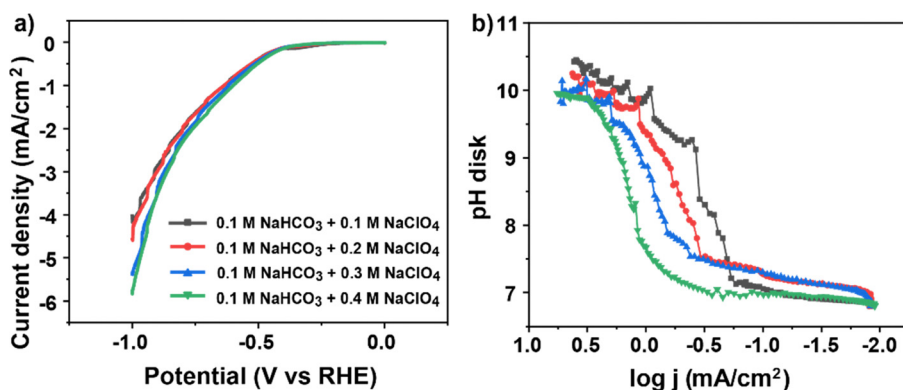

Fig. 7 (a) Cyclic voltammograms in CO_2-saturated electrolytes with different concentrations of Na$^+$ at 2 mV s^{-1} and a rotation rate of 2500 rpm. (b) Variation of the interfacial pH as a function of the logarithm of the current density during the cyclic voltammetry from (a).

decreases by the enhanced buffering ability (Fig. 7(a) and (b)). However, comparing Fig. 7 to Fig. 5, the effect is clearly less than the effect of a "real" buffer like bicarbonate.

Conclusions

In this work, we have studied the variation of the interfacial pH during CO_2RR using a real-time pH sensor based on RRDE, which has been employed to follow the interfacial pH as a function of various electrolyte parameters. CO_2RR and HER lead to the accumulation of OH^- near the electrode while the concurrent homogenous (buffer) reactions resist the corresponding pH changes.

It is observed that at low current densities, the interfacial pH is close to 7, whereas with increasing current density there is a quick shift to an interfacial pH near 10–11, as expected from the pK_a's of the buffers. Scan rate dependent experiments show that the equilibrium of the CO_2/HCO_3^- buffer is reached within *ca.* 10 s, such that at low scan rates ($\sim$2 mV s^{-1}) the buffering reactions can be considered in equilibrium and therefore the interfacial concentrations of different carbonaceous species can be calculated from the measured interfacial pH using equilibrium expressions. The experiments show that increasing mass transport, buffer capacity and the size and concentration of the cation can all help suppressing pH gradients near the electrode surface. Still, increasing buffer capacity has by far the largest effect. Increasing mass transport is not as efficient in resisting interfacial pH changes; in fact, the effect of mass transport by changing the disk rotation rate appears to be the smallest. The interfacial pH is still as high as 11 under strong forced convection (2500 rpm). Moreover, CO_2RR may not benefit from increasing buffer or cation concentration, since the competing HER is typically more enhanced by that than the CO_2RR.

We chose here to study a relatively simple system (Au electrocatalyst, producing only CO and H_2) so that we could fully focus on the influence of the electrolyte parameters. Complementing previous work from our group regarding electrolyte effects on CO_2 reduction on gold, which have been summarized in a recent review,[52] this study provides valuable new qualitative and quantitative insights on the role of the interfacial pH in the competition between CO_2 reduction and HER, and how it is affected by electrolyte properties. A key conclusion is that at on the (R)RDE, CO_2 reduction is never mass transport limited. The relevant concentration gradient in the system is built up due to the pH gradient existing between the electrode and the bulk electrolyte, and the most effective way to control this gradient is by buffering, not by improving mass transport. We expect this conclusion to be general, and transferable to more practical electrode geometries, such as gas diffusion electrodes. This conclusion should also be applicable to Cu electrodes at similar current densities and electrolyte conditions. Although the RRDE setup requires the use of a flat electrode, we have shown previously how learnings on the RDE can help in interpreting results obtained with a nanoporous electrode.[54]

Summarizing, our research illustrates a remarkable difference between the interface and the bulk, even under strong forced convection. The 4-HATP/4-NSTP modified RRDE pH probe functions as an effective tool to probe the interfacial environment, which can also be applied in other electrochemical reactions. The cation effect, anion effect, and buffering effects and their influence on the local pH, are strongly coupled with each other, and the RRDE pH probe presented here offers an excellent means for their deconvolution.

Experimental

Chemicals and materials

Electrolytes were prepared using ultrapure water ($>$18.2 MΩ cm, Millipore Milli-Q) and the following chemicals: Li_2CO_3 ($>$99.999%, trace metal basis, Thermo Fisher), $NaHCO_3$ ($>$99.7%, metal basis, anhydrous, Alfa Aesar), $KHCO_3$ ($>$99.9%, metal basis, Alfa Aesar), Rb_2CO_3 ($>$99.8%, metal basis, Merck), $NaClO_4(H_2O)_x$ ($>$99.99%, trace metal basis, Sigma-Aldrich), H_2SO_4 (96%, Merck, Suprapur). All carbonate and bicarbonate electrolytes were pre-purified in Chelex (particle size: 50–100, Merck) overnight to eliminate possible metal impurities[55] and purged with either Ar (6.0 purity, Linde, 20 min) or CO_2 (4.5 purity, Linde, 20 min for bicarbonates and 1 h for carbonates) before experiments. All the electrochemical experiments were conducted with a 4-channel Biologic potentiostat (VSP-300) and Modulated Speed Rotator (Pine Research) in a home-made single compartment electrochemical cell. The electrochemical cell and other glassware were kept in $KMnO_4$ solution (1 g L^{-1} $KMnO_4$ in 0.5 M H_2SO_4) overnight and then immersed in dilute piranha solution to remove the generated MnO_x and the residual $KMnO_4$. Before using, they were rinsed and boiled with ultrapure water five times. A ring-disk electrode (Au ring and Au disk, E6/E5 ChangeDisk, Pine Research), a Au wire (0.5 mm diameter, MaTeck, 99.9%) and a Ag/AgCl electrode (RE-1B, 3 M NaCl, Biologic, inserted in a Luggin capillary) were used as working electrode, counter electrode and reference electrode, respectively. Before being put in contact with the electrolyte, the Au counter electrode was flame annealed using a butane torch.

Preparation and modification of the electrodes

After inserting the Au disk (5.0 mm diameter) in the Au ring matrix, the RRDE tip was polished with 3 μm, 1 μm, 0.25 μm diamond suspension (MetaDi, Buehler), respectively, and sonicated in ethanol and ultrapure water for 5 min in between polishing steps. Before measurements, both ring and disk electrodes were characterized in Ar-saturated 0.1 M H_2SO_4 by cyclic voltammetry at 100 mV s^{-1} between 0 and 1.75 V *vs.* RHE (see Fig. S1a in the ESI†). The electrochemical surface area (ECSA) of the disk electrode was calculated by the ratio of the charge of the Au oxide reduction peak and the charge density of a Au oxide monolayer (386 μC cm^{-2}). Then, the Au disk was changed into a Teflon counterpart and the RRDE tip was dipped into a 1 mM 4-NTP (4-nitrothiophenol (4-NTP, Merck, 80%)

2904 | *Phys. Chem. Chem. Phys.,* 2023, **25**, 2897–2906

This journal is © the Owner Societies 2023

dissolved in ethanol (96%, absolute, VWR) solution for 20 min, during which the thiol-containing compound would self-assemble as a monolayer on the Au ring electrode. After that, the tip is rinsed with ethanol and water respectively, and dried in a N_2 flow. The Au disk was reassembled carefully and the 4-NTP on the ring was further converted to the pH sensing redox couple 4-NSTP/4-HATP *via* cyclic voltammetry in 0.1 M H_2SO_4 from 0.68 to 0.11 V *vs.* RHE at 100 mV s^{-1}. The lower vertex potential of 0.11 V *vs.* RHE is set so that the conversion efficiency is maximized (see Fig. S1b–d, ESI†).

RRDE pH measurements

The Au disk was cycled from 0 to -1.0 V *vs.* RHE in different electrolytes with a 2 mV s^{-1} scan rate while the cyclic voltammograms of the 4-HATP/4-NSTP pH sensing couple were continuously recorded with a scan rate of 200 mV s^{-1}. The potential window was adjusted when necessary, as the interfacial pH increased. Specifically, the cycling range on the ring in CO_2-saturated bicarbonate (pH 6.8) was kept to be -0.25 V to 0.15 V *vs.* Ag/AgCl until the potential on the disk reached -0.5 V *vs.* RHE. It was then changed to -0.35 V to 0.05 V *vs.* Ag/AgCl when the interfacial pH was around 9. To avoid any interference from oxygen, the gases (CO_2 or Ar) were continuously purged into the electrolyte during the measurements. Details of the calculations of the interfacial pH are given in the ESI.†

Author contributions

The manuscript was written through contributions of all authors. All authors have given approval to the final version of the manuscript.

Conflicts of interest

There are no conflicts to declare.

Acknowledgements

Notes and references

1 Y. Y. Birdja, E. Pérez-Gallent, M. C. Figueiredo, A. J. Göttle, F. Calle-Vallejo and M. T. M. Koper, *Nat. Energy*, 2019, **4**, 732–745.

2 B. A. Zhang, T. Ozel, J. S. Elias, C. Costentin and D. G. Nocera, *ACS Cent. Sci.*, 2019, **5**, 1097–1105.

3 B. Deng, M. Huang, X. Zhao, S. Mou and F. Dong, *ACS Catal.*, 2021, **12**, 331–362.

4 Y. J. Sa, C. W. Lee, S. Y. Lee, J. Na, U. Lee and Y. J. Hwang, *Chem. Soc. Rev.*, 2020, **49**, 6632–6665.

5 A. Wagner, C. D. Sahm and E. Reisner, *Nat. Catal.*, 2020, **3**, 775–786.

6 A. S. Malkani, J. Anibal and B. Xu, *ACS Catal.*, 2020, **10**, 14871–14876.

7 M. C. O. Monteiro, F. Dattila, N. Lopez and M. T. M. Koper, *J. Am. Chem. Soc.*, 2022, **144**, 1589–1602.

8 M. C. O. Monteiro, F. Dattila, B. Hagedoorn, R. García-Muelas, N. López and M. T. M. Koper, *Nat. Catal.*, 2021, **4**, 654–662.

9 H. Hashiba, L.-C. Weng, Y. Chen, H. K. Sato, S. Yotsuhashi, C. Xiang and A. Z. Weber, *J. Phys. Chem. C*, 2018, **122**, 3719–3726.

10 G. Marcandalli, A. Goyal and M. T. M. Koper, *ACS Catal.*, 2021, **11**, 4936–4945.

11 G. Marcandalli, M. Villalba and M. T. M. Koper, *Langmuir*, 2021, **37**, 5707–5716.

12 K. J. P. Schouten, E. Pérez Gallent and M. T. M. Koper, *J. Electroanal. Chem.*, 2014, **716**, 53–57.

13 A. S. Varela, M. Kroschel, N. D. Leonard, W. Ju, J. Steinberg, A. Bagger, J. Rossmeisl and P. Strasser, *ACS Energy Lett.*, 2018, **3**, 812–817.

14 Z. Zhang, L. Melo, R. P. Jansonius, F. Habibzadeh, E. R. Grant and C. P. Berlinguette, *ACS Energy Lett.*, 2020, **5**, 3101–3107.

15 A. Goyal and M. T. M. Koper, *Angew. Chem., Int. Ed.*, 2021, **60**, 13452–13462.

16 X. Lu, C. Zhu, Z. Wu, J. Xuan, J. S. Francisco and H. Wang, *J. Am. Chem. Soc.*, 2020, **142**, 15438–15444.

17 R. E. Zeebe and D. Wolf-Gladrow, *CO2 in seawater: equilibrium, kinetics, isotopes*, Gulf Professional Publishing, 2001.

18 K. G. Schulz, U. Riebesell, B. Rost, S. Thoms and R. E. Zeebe, *Mar. Chem.*, 2006, **100**, 53–65.

19 M. Dunwell, X. Yang, B. P. Setzler, J. Anibal, Y. Yan and B. Xu, *ACS Catal.*, 2018, **8**, 3999–4008.

20 M. C. O. Monteiro, A. Mirabal, L. Jacobse, K. Doblhoff-Dier, S. C. Barton and M. T. M. Koper, *JACS Au*, 2021, **1**, 1915–1924.

21 K. Yang, R. Kas and W. A. Smith, *J. Am. Chem. Soc.*, 2019, **141**, 15891–15900.

22 M. C. O. Monteiro, A. Goyal, P. Moerland and M. T. M. Koper, *ACS Catal.*, 2021, **11**, 14328–14335.

23 M. R. Singh, Y. Kwon, Y. Lum, J. W. Ager, 3rd and A. T. Bell, *J. Am. Chem. Soc.*, 2016, **138**, 13006–13012.

24 L. D. Chen, M. Urushihara, K. Chan and J. K. Nørskov, *ACS Catal.*, 2016, **6**, 7133–7139.

25 A. Frumkin, *Trans. Faraday Soc.*, 1959, **55**, 156–167.

26 A. Goyal and M. T. M. Koper, *J. Chem. Phys.*, 2021, **155**, 134705.

27 G. Marcandalli, K. Boterman and M. T. M. Koper, *J. Catal.*, 2022, **405**, 346–354.

28 M. C. O. Monteiro and M. T. M. Koper, *Curr. Opin. Electrochem.*, 2021, **25**, 100649.

29 B. P. Nadappuram, K. McKelvey, R. Al Botros, A. W. Colburn and P. R. Unwin, *Anal. Chem.*, 2013, **85**, 8070–8074.

30 V. S. Joshi, P. S. Sheet, N. Cullin, J. Kreth and D. Koley, *Anal. Chem.*, 2017, **89**, 11044–11052.

31 M. C. O. Monteiro, L. Jacobse and M. T. M. Koper, *J. Phys. Chem. Lett.*, 2020, **11**, 9708–9713.

32 M. C. O. Monteiro, L. Jacobse, T. Touzalin and M. T. M. Koper, *Anal. Chem.*, 2020, **92**, 2237–2243.

33 R. Song, Q. Xiong, T. Wu, X. Ning, F. Zhang, Q. Wang and P. He, *Anal. Bioanal. Chem.*, 2020, **412**, 3737–3743.

34 M. Etienne, P. Dierkes, T. Erichsen, W. Schuhmann and I. Fritsch, *Electroanalysis*, 2007, **19**, 318–323.

35 C. Lindino and L. Bulhoes, *Anal. Chim. Acta*, 1996, **334**, 317–322.

36 H. E. Lackey, G. L. Nelson, A. M. Lines and S. A. Bryan, *Anal. Chem.*, 2020, **92**, 5882–5889.

37 O. Ayemoba and A. Cuesta, *ACS Appl. Mater. Interfaces*, 2017, **9**, 27377–27382.

38 C. Zong, M. Xu, L. J. Xu, T. Wei, X. Ma, X. S. Zheng, R. Hu and B. Ren, *Chem. Rev.*, 2018, **118**, 4946–4980.

39 W. Albery, *Trans. Faraday Soc.*, 1966, **62**, 1915–1919.

40 A. M. Zimer, M. Medina da Silva, E. G. Machado, H. Varela, L. H. Mascaro and E. C. Pereira, *Anal. Chim. Acta*, 2015, **897**, 17–23.

41 Y. Yokoyama, K. Miyazaki, Y. Miyahara, T. Fukutsuka and T. Abe, *ChemElectroChem*, 2019, **6**, 4750–4756.

42 M. C. O. Monteiro, X. Liu, B. J. L. Hagedoorn, D. D. Snabilié and M. T. M. Koper, *ChemElectroChem*, 2021, **9**, e202101223.

43 W. J. Albery and E. J. Calvo, *J. Chem. Soc., Faraday Trans. 1*, 1983, **79**, 2583–2596.

44 P. Steegstra and E. Ahlberg, *J. Electroanal. Chem.*, 2012, **685**, 1–7.

45 B. M. Tackett, D. Raciti, N. W. Brady, N. L. Ritzert and T. P. Moffat, *J. Phys. Chem. C*, 2022, **126**, 7456–7467.

46 Y. Yokoyama, K. Miyazaki, Y. Kondo, Y. Miyahara, T. Fukutsuka and T. Abe, *Chem. Lett.*, 2020, **49**, 195–198.

47 F. Zhang and A. C. Co, *Angew. Chem., Int. Ed.*, 2020, **59**, 1674–1681.

48 G. Marcandalli, M. C. O. Monteiro and M. T. M. Koper, *Phys. Chem. Chem. Phys.*, 2022, **24**, 2022–2031.

49 P. Steegstra and E. Ahlberg, *Electrochim. Acta*, 2012, **76**, 26–33.

50 L. J. Henderson, *Am. J. Physiol.*, 1908, **21**, 173–179.

51 H. Zhong, K. Fujii, Y. Nakano and F. Jin, *J. Phys. Chem. C*, 2014, **119**, 55–61.

52 G. Marcandalli, M. C. O. Monteiro, A. Goyal and M. T. M. Koper, *Acc. Chem. Res.*, 2022, **55**, 1900–1911.

53 A. Goyal, G. Marcandalli, V. A. Mints and M. T. M. Koper, *J. Am. Chem. Soc.*, 2020, **142**, 4154–4161.

54 A. Goyal, C. J. Bondue, M. Graf and M. T. M. Koper, *Chem. Sci.*, 2022, **13**, 3288–3298.

55 E. W. Davey, J. H. Gentile, S. J. Erickson and P. Betzer, *Limnol. Oceanogr.*, 1970, **15**, 486–488.